Nuclear Science and Techniques (2025) 36:16
https://doi.org/10.1007/s41365-024-01605-z

Boron shielding design for neutron and gamma detectors of a pulsed neutron tool

Xin-Yang Wang[1] · Jun-Yan Chen[1] · Qiong Zhang[1]

Received: 10 April 2024 / Revised: 23 May 2024 / Accepted: 27 May 2024 / Published online: 20 December 2024

Abstract
Shielding materials are critical for downhole pulsed neutron tool design because they directly influence the accuracy of formation measurements. A well-designed shield configuration ensures that the response of the tool is maximally representative of the formation without being affected by the tool and borehole environment. This study investigated the effects of boron-containing materials on neutron and gamma detectors based on a newly designed logging-while-drilling tool that is currently undergoing manufacturing. As the boron content increased, the ability to absorb thermal neutrons increased significantly. Through simulation, it was proven that boron carbide (B_4C)can be used as an effective boron shielding material for thermal neutrons, and is therefore employed in this work. To shield against thermal neutrons migrating from the mud pipes, the optimal shielding thicknesses for the near- and far-neutron detectors were determined to be 5 and 4 mm. At a porosity of 25 p.u., near-neutron sensitivity exhibited a 5.6% increase. Furthermore, to shield the capture gamma generated by thermal neutrons once they enter the tool from the mud pipe and formation, internal and external shields for the gamma detector were evaluated. The results show that the internal shield requires a boron content of 75%, whereas the external shield has a thickness of 14.2 mm thickness and a boron content of 25% to minimize the tool effect.

Keywords Nuclear well logging · Pulsed neutron tool · Boron shielding

1 Introduction

In petroleum exploration and development, a chemical source is commonly used for nuclear well logging. This technique employs Cs137 or AmBe sources to assess the formation properties [1, 2]. However, concerns persist regarding the environmental pollution risks posed by chemical sources during transportation and measurement. Consequently, pulsed neutron well logging, noted for its safety and controllability, has emerged as a viable alternative to traditional well logging.

Pulsed neutron logging is indispensable for evaluating complex oil and gas reservoirs. It relies on a pulsed neutron generator, which is an electronically controlled small-accelerator neutron source. By adjusting the pulse emission frequency, it can achieve integrated measurements [3] of multiple formation parameters, such as density, porosity, and lithology [4]. Although pulsed neutron logging reduces radioactive risks and provides richer formation information than traditional well logging through a single measurement, the strong penetration capability of high-energy neutrons and the variable distribution of secondary gamma rays may have a mutual influence on gamma or neutron detection [5–8], especially in LWD measurements, where particles may penetrate through mud pipes and reach the detectors. Consequently, there may be a higher level of tool-related information included in the detector-recorded information, thereby reducing the proportion of formation responses. To reduce non-formation-related information, tool shielding must be studied. To understand the rationale behind shielding design requires the review of the principles of pulsed neutron logging.

This work was supported by the Natural Science Foundation of China (Nos. U23B20151 and 52171253).

✉ Qiong Zhang
zhanqio@uestc.edu.cn

[1] University of Electronic Science and Technology of China, Chengdu 611731, China

1.1 Overview of pulsed neutron well-logging principle

In pulsed neutron logging, taking a D-T source as an example, after the emission of 14 MeV fast neutrons, the initial energy loss of the neutrons occurs mostly because of inelastic collisions [9]. During neutron deceleration, multiple inelastic collisions may occur, resulting in inelastic scattering rays with characteristic energies specific to different elements. As fast neutrons decelerate to thermal neutrons and are absorbed by target nuclei in geological formations, characteristic energy-capturing gamma rays are emitted. The elemental composition of geological formations can be determined by analyzing the energy spectra of these two types of gamma rays [10].

Simultaneously, as the neutron energy decreases, elastic collisions gradually become dominant during neutron deceleration. During elastic collisions, the neutron energy is transferred to the target nucleus in a manner consistent with the conservation of kinetic energy within the system, as shown in Eq. 1.

$$E_M = E_{\mathrm{n}} - E'_{\mathrm{n}} = \frac{4Mm}{(M+m)^2} E_{\mathrm{n}} \cos\theta^2. \tag{1}$$

The kinetic energy of the recoil nucleus is denoted as E_M, the kinetic energy of the neutron before the collision is E_{n}, and the kinetic energy after the collision is E'_{n}. The masses of the recoil nucleus and neutrons are denoted as m and M, respectively. The angle between the recoil nucleus and incident neutron direction is θ. Therefore, when neutrons collide with hydrogen atoms, they experience maximum energy loss. Hydrogen is commonly found in water, oil, gas, and other substances. The formation porosity can be inferred when neutrons are decelerated to thermal energy by hydrogen atoms and subsequently detected by detectors [4].

1.2 Motivation for investigating boron shielding

When designing pulsed neutron tools, several types of detectors must be incorporated to enable various measurement modes within a single tool. LWD tools differ from cable tools because of the inclusion of a mud pipe, which can lead to thermal neutron leakage and the subsequent generation of captured gamma rays when the tool elements capture these neutrons. To illustrate the effect of the described physical processes on downhole detection, as shown in Fig. 1, we considered a pulsed neutron tool comprising one neutron detector and one gamma-ray detector with a mud pipe. Figure 1 outlines the potential physical pathways that particles reaching the detectors might traverse, as indicated by paths ①–⑦. For neutrons, the possible paths include ①–④. Gamma is summarized as paths ⑤–⑦.

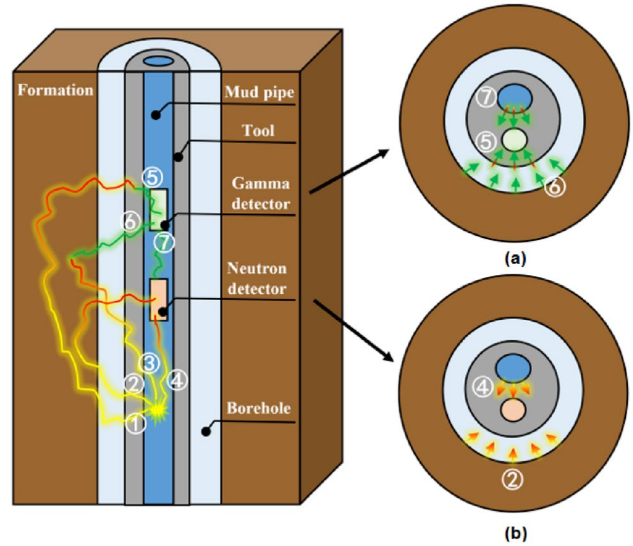

Fig. 1 (Color online) Path diagram of n-γ physic reactions in pulsed neutron well-logging tool. **a** Gamma detector x-y section; **b** Neutron detector x-y section

Path ① and Path ③: After the 14 MeV neutrons are generated, they are moderated through the tool, borehole, and formation, forming thermal neutrons in the formation and subsequently in the tool. Path ②: After the 14MeV neutrons are generated from the source, they are moderated through the tool, borehole, and formation, after which the thermal neutrons formed are captured by the neutron detector. Path ④: Fast neutrons generated from the source may be directly moderated within the tool (including the mud pipe) and ultimately detected using neutron detectors. Path ⑤: Following path ①, the neutrons returning to the tool generate captured and inelastic gamma rays. Path ⑥: This is similar to Path ⑤, but the generation of captured and inelastic gamma rays occurs within the formation. Path ⑦:The neutrons that follow path ④ generate both captured and inelastic gamma rays inside the tool.

For Path ④, neutrons might be detected directly without interacting with the formation, which is disadvantageous for measuring formation porosity. In gamma paths ⑤ and ⑦, gamma rays generated within the tool (including the mud pipe) need to be shielded, especially for common tool elements like Fe, Ni, and Mn, as tool-related contributions could lead to inaccuracies in determining the formation's elemental content [11–13]. This issue arises because the tool's spectrum may overshadow formation data, resulting in inaccuracies or incomplete subtraction of the tool's spectrum, thereby complicating elemental measurement.

Therefore, one feasible approach in spectrum analysis is to reduce the contribution of tool body elemental composition [14–16]. However, once fast neutrons emitted from the tool enter the formation, inelastic gamma-ray generation is inevitable, and these inelastic gamma rays produced by the tool cannot be eliminated through shielding [17]. Thus, for elemental measurement, it is crucial to shield the potential thermal neutrons that may undergo neutron capture reactions with the tool, such as by implementing shielding around the tool or mud pipe to prevent direct interactions of thermal neutrons with tool elements.

Boron is an important element in neutron shielding as it has a high thermal neutron absorption cross section [18, 19]. Compared to other elements commonly used for neutron shielding, such as cadmium and gadolinium, boron releases relatively low gamma energy during the capture process, which can be removed by lower energy truncation. These characteristics render boron an effective shielding material. Previous studies [20–28] have demonstrated the feasibility of using Monte Carlo simulation software for tool design. These studies indicate that there are various materials available for thermal neutron shielding [29], including some novel materials [30–33], which exhibit both gamma and neutron shielding properties and are used in applications such as ionizing radiation shielding and medical diagnostics. Additionally, materials like boron concrete, borated polyethylene [34], and boron-containing stainless steel are employed in fields such as laboratory shielding [35] and nuclear power plant shielding [36]. However, high temperature and pressure in the downhole environment, along with tool volumetric constraints, pose new challenges for more effective shielding.

The primary challenge in well-logging tool shielding involves two key considerations. First, the spatial limitations of the tool restrict the use of thick shielding layers to block high-energy neutrons, requiring materials with high shielding efficiency to achieve maximum effectiveness within a compact space. Second, selecting appropriate shielding materials necessitates evaluating factors such as melting point, tensile strength, and hardness, allowing for a broader range of materials that can withstand high temperatures and complex structural demands within the tool.

This study investigates the design of boron-containing shielding for an LWD pulsed neutron tool, focusing on its impact on neutron and gamma detection. Monte Carlo simulations were used to examine various shielding materials and thicknesses around the neutron detector, assessing their effects on neutron count rates and ratios. Additionally, the internal and external shielding of the gamma detector was evaluated to determine its influence on gamma energy spectra and count rates. The aim of this study is to provide a reference framework for designing shielding in pulsed neutron logging tools.

2 Pulsed neutron tool design

2.1 Monte Carlo modeling of the tool

The open-source Monte Carlo simulation software Geant4 (Geometry and Tracking 4) was used for evaluation [37]. This study employed a pulsed neutron logging tool currently under development. This tool can acquire critical formation parameters, such as elemental composition, density, and porosity. For integrated detection, both gamma and neutron detectors were included. To simulate pulsed neutron tool detection, the source was defined as a 14 MeV pulsed neutron source in Geant4. The detailed model is shown in Fig. 2.

To differentiate the origins of the particles detected, the data processing in Geant4 is illustrated in Fig. 2. During particle transport, the type of particle produced is identified by calling the *SteppingAction*, such as gamma rays produced by neutron inelastic collisions or capture reactions. Subsequently, based on *GetVertexPosition*(), the position, called *logicalVolume*, where the gamma was generated is determined, such as formations, boreholes, tools, or mud pipes. If the particle reaches the detector, it is logged into *HistoManager*, enabling subsequent result output.

2.2 Neutron detector shields

The tool incorporates an internal mud pipe, primarily for transporting drilling mud during logging. After fast neutrons are emitted, thermal neutrons may travel directly to the neutron detectors via the mud pipe. To shield against these neutrons, neutron shielding is typically installed at the bottom of the neutron detectors within the tool, as shown in Fig. 2. The neutron detector was enveloped by three layers: the bottom layer was a neutron shield; the middle layer contained the detectors within an aluminum alloy detector room; and the top layer was an aluminum alloy detector shell.

To prepare boron compounds suitable for engineering applications, they must be processed into solid forms. However, boron compounds are inherently brittle and exhibit low solubility in steel, making the preparation of high-boron steel challenging as boron content increases. Therefore, to select the optimal shield material, three materials were evaluated for their impact on neutron measurements.

- *Aluminum-Boron Carbide* (Al-B_4C) With a density of 2.6 g/cm^3, this composite material contains 40% B_4C and 60% aluminum. It has a hardness range of 300–400 GPa and a melting point range of 190 – 200 °C [38].
- *Boron Carbide* B_4C is known for its high structural strength, this material has a density of 2.52 g/cm^3 with

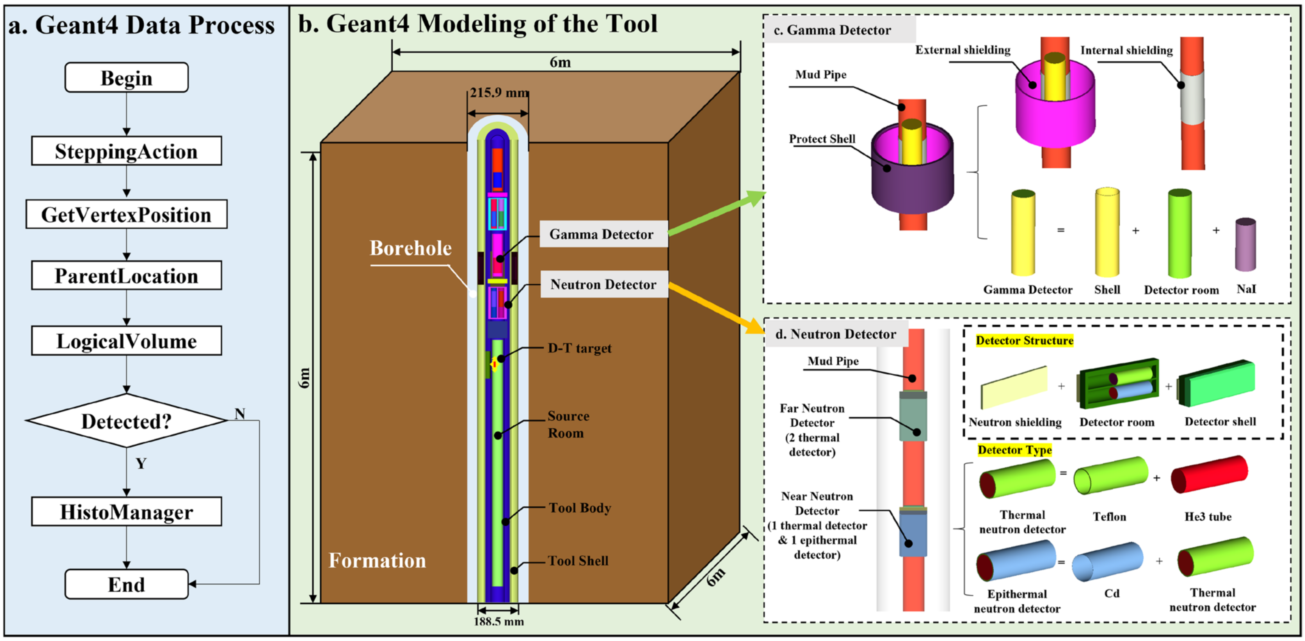

Fig. 2 (Color online) Multi-detector pulsed neutron tool's construction in Geant4

a composition of B10 (76.9%) and C (23.1%). It exhibits a high hardness of 500 GPa and a melting point of 2350 °C [39, 40].

- *Aluminum-Boron Alloy* (Al-B) Al-B alloys are renowned for their high strength, excellent corrosion resistance. Selected material [41, 42] with a density of 2.45 g/cm^3, including B10 (11%), Si (0.3%), Fe (0.35%), Ti (0.08%), K (1%), Na (0.5%), and Al (86.77%). Its hardness is in the range of 100–200 GPa with a tensile strength of 220–250 MPa and a melting point between 690 – 700 °C.

2.3 Shields of gamma detector

In this tool, a far-gamma detector was used for density measurements, whereas a near-gamma detector was used for elemental measurements. The near-gamma detector consists of two shields: one shields against thermal neutrons migrating from the mud pipe, and the other shields against thermal neutrons migrating from outside the tool, as shown in Fig. 2.

Due to challenges in shaping pure boron and its high cost, this study used HNBR rubber mixed with boron for the external shielding of the tool. Given the structural constraints, the maximum thickness of the internal shielding was limited to 1.1 mm, thus a pure boron material was selected for internal shielding. Subsequent sections will focus on optimizing the shielding for the near-gamma detector and investigating the effects of different thicknesses and boron contents in both the internal and external shields on spectral elemental measurements.

3 Results analysis and discussion

This section presents a shielding design study based on the tool described above. To investigate the influence patterns of neutron and gamma detection in the tool, detector responses were obtained by altering the boron material and its thickness. A population of 10^8 particles was simulated. The tool was positioned centrally in the sandstone formation.

3.1 Shield design of neutron detector

3.1.1 Neutron spatial distribution analysis

This section first analyzes the distribution of thermal and fast neutrons inside the mud pipe. In Geant4, the *X-Z* cross section of the mud pipe was extracted for flux analysis, as shown in Fig. 3a.

The source-to-detector distances for the two neutron detectors are 28.8 cm and 69.2 cm, respectively. As shown in Fig. 3b, the number of low-energy neutrons (<1 MeV) decreases sharply as the source-to-detector distance increases. In Fig. 3c, the distribution of fast neutrons is primarily concentrated around the source. After emission, these fast neutrons are quickly moderated by the surrounding media, resulting in minimal distribution within the mud pipe, tool, and borehole, making it difficult for them to reach the near- and far-neutron detectors. In contrast, thermal neutrons, as shown in Fig. 3d, exhibit a distribution within the mud pipe that differs significantly from that of fast neutrons. Near the neutron detector, the number of thermal neutrons

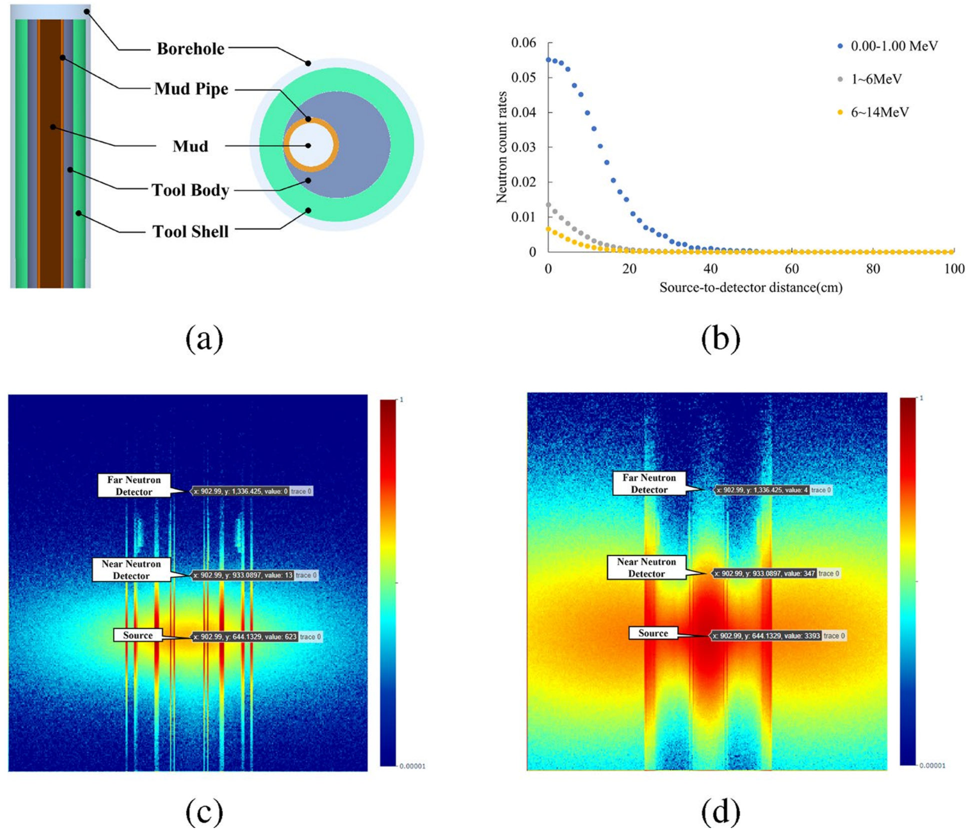

Fig. 3 (Color online) Neutron spatial distributions. **a** *X-Z* and *X-Y* sections; **b** neutron distribution of different energy; **c** fast neutron distribution; **d** thermal neutron distribution

originating from the mud pipe decreases by approximately 9.7 times. Without adequate shielding, near-neutron detectors are significantly affected. In contrast, the far-source neutron detector is less affected, as the thermal neutrons inside the mud pipe are insulated from the external environment, allowing for different shielding designs for detectors at varying source-to-detector distances.

3.1.2 Material comparison

This section analyzes the performance of the three shielding materials, B_4C, Al-B_4C, and Al-B alloy, focusing on the near-neutron count rate, near epithermal neutron count rate, far-neutron count rate, and neutron ratio (the ratio of the near detector count rate to the far detector count rate) under different porosities, as shown in Fig. 4. For neutron porosity measurements, the detection sensitivity S is defined as Eq. 2.

$$S = \frac{\partial R}{R \partial \emptyset}. \tag{2}$$

The thermal neutron count ratio is defined as R, and the formation porosity is $\emptyset$. At the location of the far-neutron detector shown in Fig. 4b, the thermal neutron flux is relatively low, indicating that fewer neutrons are received from the mud pipe and that the thermal neutron count is predominantly influenced by the formation. Consequently, as porosity changes, the far-neutron detector counts remain comparable across all three materials. In contrast, as shown in Fig. 4a, the near detector is more significantly affected by thermal neutrons within the mud pipe. Among the materials, the AlB alloy has the lowest boron content at 11%, whereas B_4C has the highest boron content at 76%, making B_4C the most effective at absorbing thermal neutrons. Consequently, with B_4C shielding, the count rates for near-thermal and epithermal neutrons are the lowest, as shown in Fig. 4c. Although the AlB alloy results in a higher near-source count rate, leading to a larger detector ratio, as seen in Fig. 4e, the AlB alloy has the lowest sensitivity, while B_4C achieves the highest sensitivity response.

This phenomenon occurs because, with low-boron-content shielding, the detector receives an overwhelming amount of non-formation information, making it less sensitive to changes in formation porosity. The recommended materials in this study remain B_4C and Al-B_4C. Based on the trend in near detector count changes with porosity, B_4C provides the best shielding performance, while Al-B_4C is a viable alternative to B_4C.

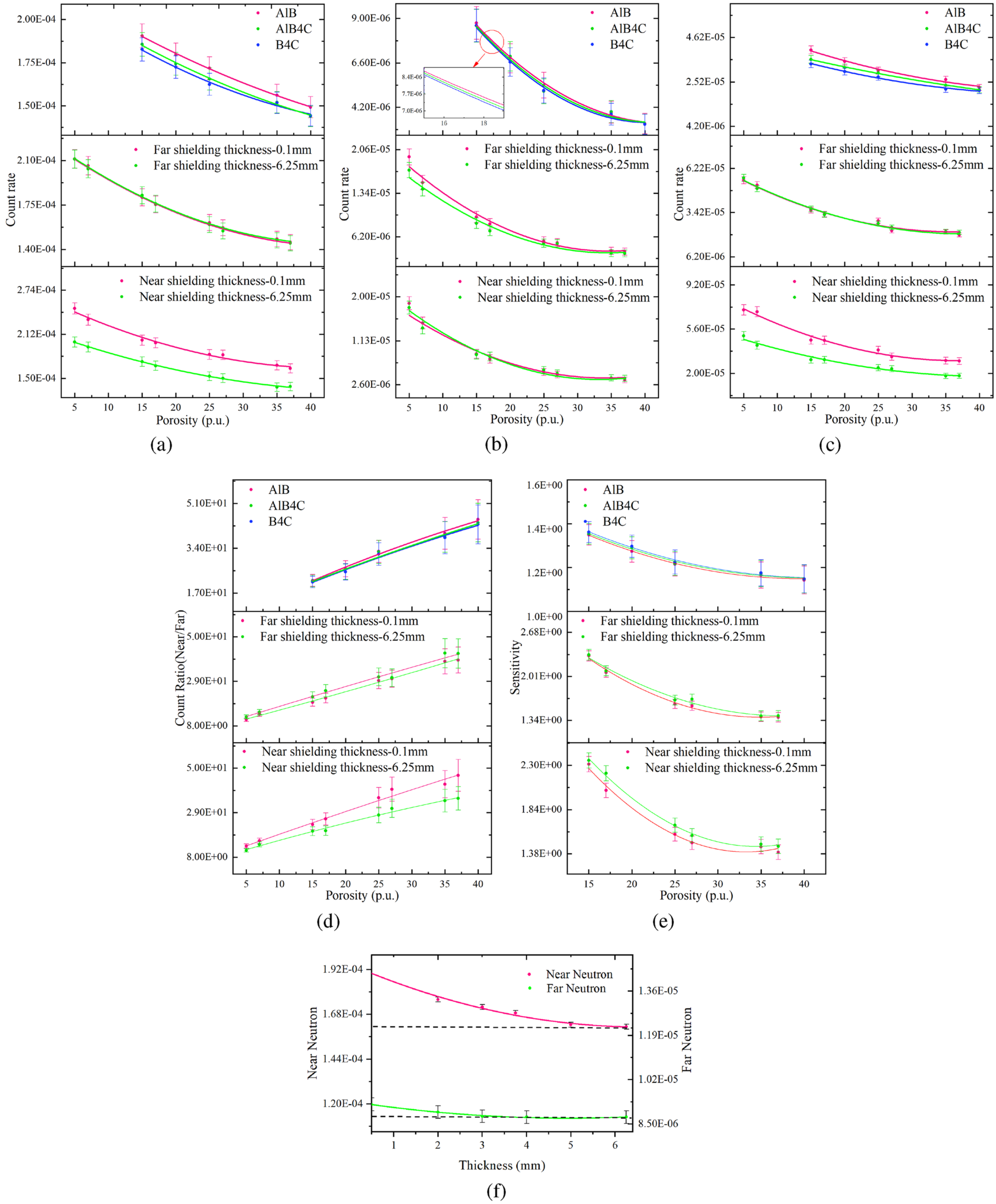

Fig. 4 (Color online) Comprehensive analysis of neutron measurements under various conditions. **a** Near-neutron detector; **b** far-neutron detector; **c** thermal neutron detector; **d** count ratio; **e** sensitivity; **f** near- and far-neutron count rate with various thicknesses

3.1.3 The effect of shielding thickness

With B_4C identified as the optimal shielding material, its effectiveness was evaluated at various thicknesses to observe changes in the neutron detector count rate. Figure 4 compares near- and far-neutron detectors at different shielding thicknesses. Changes in the shielding thickness of one detector did not affect the count pattern of the other. For detectors at two source distances, as porosity increases, the capacity of the formation to moderate neutrons is enhanced, resulting in a shorter moderation length, and consequently, fewer neutrons returning to the detectors. Consequently, the overall count rate decreases. Neutrons transmitted through the mud pipe remain unaffected by the surrounding environment; therefore, their counts stay constant. For the near-neutron detector, as shown in Fig. 4a, changing the shielding thickness results in a noticeable reduction in the count rate. In the far-neutron detector, shown in Fig. 4b, the differences gradually diminish with increasing porosity and tend to converge. This convergence occurs because, as formation information decreases, the proportion of non-formation information increases, potentially preventing the distant detector from accurately identifying formation information at high porosities.

Sensitivity variations in the near and far detectors for different thicknesses are shown in Fig. 4e. It can be observed that the thicker the shielding, the lower the sensitivity. For example, at a porosity of 25 p.u., the sensitivities of the near detector with shielding thicknesses of 0.1 mm and 6.25 mm are 1.58 and 1.67, respectively, indicating a 5.6% increase in sensitivity response. Figure 4f illustrates the count rate variations for both detectors at different shielding thicknesses. It is notable that the count rate for the far detector gradually stabilizes at a shielding thickness of 4 mm, with the neutron contribution mainly from the tool background and formation. In contrast, the count rate for the near-neutron detector stabilizes at a thickness of 5 mm. Therefore, for optimal neutron shielding design, a 5-mm thickness was selected for the near-neutron detector, and a 4-mm thickness for the far-neutron detector.

3.2 Shield design of gamma detector

3.2.1 Gamma spatial distribution analysis

To design an optimal gamma shield, it is essential to understand the distribution of gamma rays. Inelastic gamma rays are generated by high-energy neutrons through inelastic collisions, while captured gamma rays are produced by the capture of thermal neutrons. Thus, after neutrons pass through the mud pipe and tool, gamma information unrelated to the formation is generated. Figure 5a and b shows the distribution of captured and inelastic gamma rays generated within the mud pipe, while Fig. 5c and d illustrates the distribution of captured and inelastic gamma rays generated within the tool.

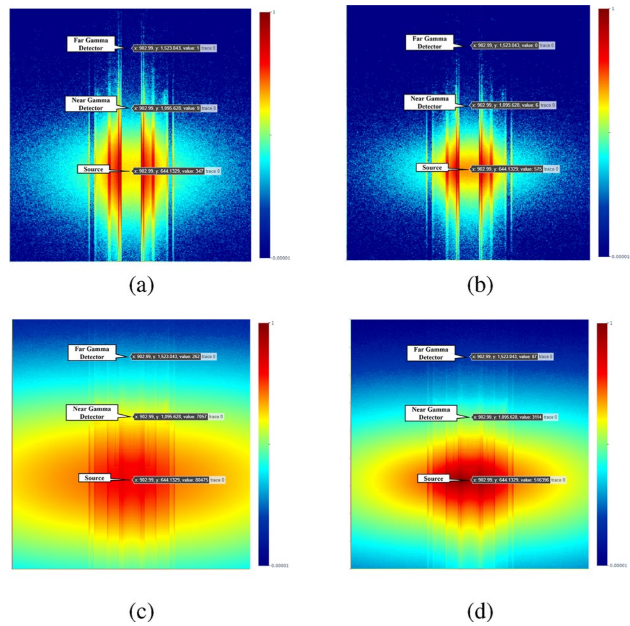

Fig. 5 (Color online) Gamma spatial distribution. **a** Capture gamma (mud pipe); **b** inelastic gamma (mud pipe); **c** capture gamma (tool); **d** inelastic gamma (tool)

The source-to-detector distances for the gamma detectors were 45.1 cm and 87.8 cm, respectively. Within the mud pipe, as shown in Fig. 5a and b, the distribution of captured gamma rays is broader, whereas the inelastic gamma rays are primarily concentrated near the source. Additionally, as indicated in Fig. 3d, few captured gamma rays originate from the mud pipe. This is because the likelihood of hydrogen within the mud pipe undergoing capture reactions is lower than that of metal within the tool. However, as shown in Fig. 5c and d, a significant number of both captured and inelastic gamma rays are generated inside the tool. For the capture gamma flux, the attenuation at the near-gamma detector is approximately 11.4 times that at the source, while the inelastic gamma rays decrease by a factor of 165. The attenuation of captured gamma rays is therefore less pronounced than that of inelastic gamma rays. Consequently, it is necessary to block the thermal neutrons passing through the mud pipe and reacting with the tool to reduce tool-related captured gamma contributions.

3.2.2 The effect of boron content

To evaluate the impact of boron shielding on gamma detection, this section examines variations in gamma count rates and energy spectra across shields with boron contents ranging from 0.1% to 99.9%. The thicknesses of the external and internal shielding were set to 10 mm and 1 mm, respectively. Figure 6 illustrates the proportional contributions of captured and inelastic gamma rays originating from the formation, tool, mud pipe, and borehole. The gamma contribution from the tool constitutes a significant portion, and therefore, needs to be reduced with an effective shield design. Due to the different physical mechanisms involved in generating inelastic versus captured gamma rays, the count rate of inelastic gamma rays remains relatively stable. However, for captured gamma rays, as boron content increases, the proportional contribution from the formation gradually rises, while the contribution from the tool decreases. For internal shielding, once the boron content reaches 75%, further increases do not significantly impact the count rate, as shown in Fig. 6a. At this level, the total count response from the formation increases by 2.93%, making a boron content of 75% the optimal choice for internal shielding material.

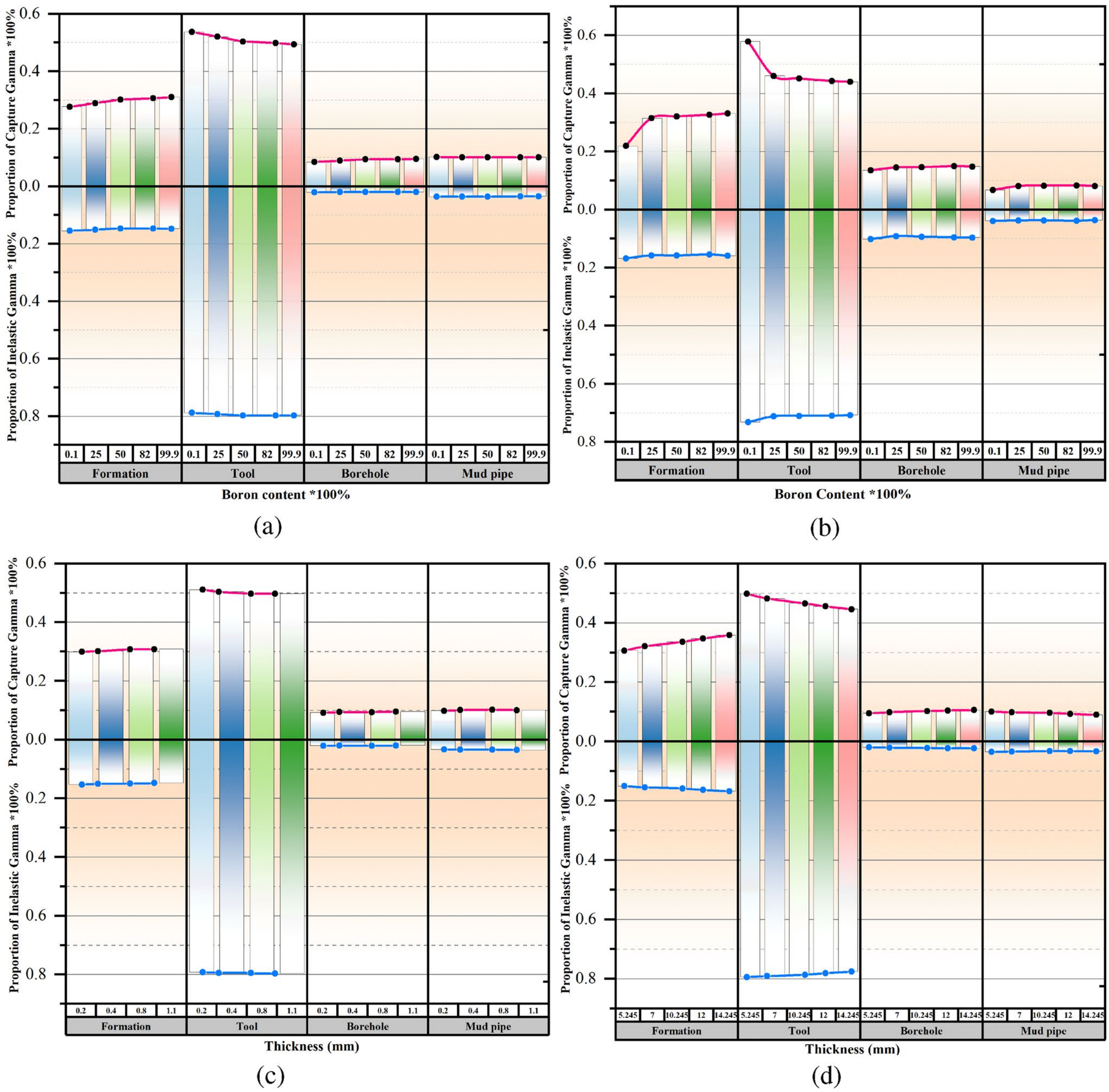

Fig. 6 (Color online) Comprehensive analysis of gamma measurements under various conditions. **a** Gamma count with different internal shield boron contents; **b** gamma count with different external shield boron contents; **c** gamma count with different internal shield thicknesses; **d** gamma count with different external shielding thicknesses

Additionally, adjusting boron content in the external shield can achieve more effective shielding, as shown in Fig. 6b. When the external boron content reaches 25%, further increases no longer significantly enhance the shielding effect, with the formation's contribution increasing by 9.56%.

3.2.3 The effect of shielding thickness

Figure 6c and d illustrates the changes in the proportional contributions of captured gamma rays from the formation, tool, mud pipe, and borehole as the thickness of the shielding increases. However, within the internal shielding, the increase in thickness did not significantly enhance the contribution of the formation to the capture of gamma rays, as shown in Fig. 6c, especially compared to the impact of boron content, as demonstrated in Fig. 6a. Therefore, for this shielding application, employing a method such as spraying boron powder could be a viable alternative to fabricating a geometric shield.

Figure 6d shows that the changes in the gamma contributions of the external shielding increase as the thickness varies from 5.2 mm to 14.2 mm. As the thickness of the external shielding increases, the proportion contributed by the mud pipe decreases approximately proportionally, whereas the proportion from the formation increases linearly.

The different trends in internal and external shielding are due to the fact that internal shielding primarily prevents thermal neutrons from the mud pipe from entering the tool, and the contribution of thermal neutrons from the mud pipe remains constant. Therefore, complete shielding of the mud pipe can be achieved at a certain level of shielding. In contrast, external shielding prevents thermal neutrons from entering the tool, and there are generally more thermal neutrons from the formation than from the mud pipe. Consequently, the shielding performance improves with increased thickness. This indicates that, for external shielding, a thicker setup is generally more beneficial. Within the constraints of the tool size, a maximum thickness of 14.2 mm was chosen, at which point the contribution from the formation increased by 5.18%.

3.2.4 Analysis on the gamma spectra

Figure 7a and b illustrates the near-gamma detector's *X-Y* plane distribution and the spectra received by the near-gamma detector. There was significant diffusion of thermal neutrons into the interior of the tool from the outside and the mud pipe, leading to neutron capture by the tool's elements and thereby generating interference. With the addition of boron to both the external and internal shielding, a noticeable reduction in the diffusion of thermal neutrons was observed, resulting in a lower neutron distribution inside the tool. The increased number of thermal neutrons in both external and internal shielding indicates an enhanced absorption effect of boron.

The tool was made of stainless steel and contained high amounts of Fe and Ni. Therefore, without thermal neutron shielding, the gamma spectrum of the tool contained distinct peaks for Fe and Ni. The Fe peaks are located at 7.1 MeV and 7.6 MeV, while the Ni peak is at 6.6 MeV. In the captured gamma distribution transmitted through the mud pipe, contributions from iron and nickel can also be observed. In terms of count rate contributions, the order is tool > formation > mud pipe > borehole. Therefore, when the contributions from these four sections are combined, the information from the formation may be overshadowed by the tool information, making it difficult to analyze the formation elements. However, in the gamma spectrum, after implementing the shielding design, the contributions from both the tool and mud pipe were significantly reduced, demonstrating the effectiveness of the shielding.

4 Conclusion

This study investigated a boron-containing shielding design for a newly developed pulsed neutron logging tool. The findings revealed that the impact of the mud pipe on the detector is significant and cannot be ignored. After fast neutrons are emitted, they slow down quickly due to the water in the mud pipe, resulting in the accumulation of a considerable amount of thermal neutrons. Since thermal neutrons in mud pipes do not provide formation information, both neutron and gamma detectors are significantly affected; therefore, an advanced shielding strategy is necessary.

First, for neutron detectors, simulations show that shielding materials with higher boron content, such as boron carbide, can achieve improved shielding effects. Considering the tool's volumetric constraints, the distribution of neutrons, and the performance of the shielding thickness, the selected shielding thicknesses for the near- and far-neutron detectors were 5 mm and 4 mm, respectively. From the thickness comparison, at a porosity of 25 p.u., the near-neutron sensitivity shows a 5.6% increase in response.

Second, for the near-gamma detector, shielding thermal neutrons is equally important to prevent the tool-related capture of gamma rays produced when thermal neutrons enter the tool. Both internal and external shields were designed. Due to volumetric constraints, it is difficult to adjust the internal shield thickness, necessitating the use of a high-concentration boron powder coating with a boron content of 75%. Moreover, the thickness of the external shield can be increased, allowing for greater flexibility in design. The simulation shows that the optimal thickness is 14.2 mm with 25% boron content to minimize the tool effect. This manuscript provides references

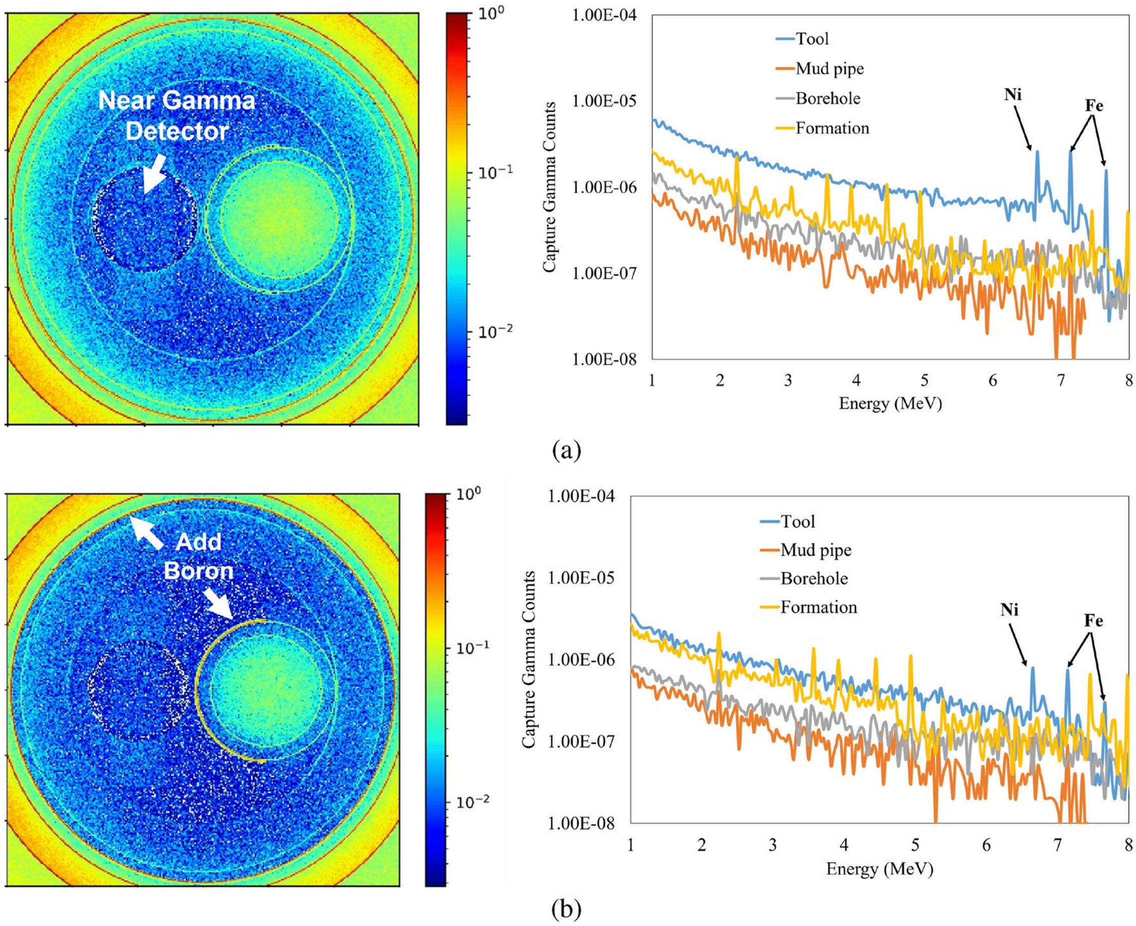

Fig. 7 (Color online) Comparative analysis of gamma and neutron distributions with and without shielding. **a** Capture gamma spectra without boron material; **b** capture gamma spectra with boron-containing shielding

and insights into the neutron and gamma shielding design of pulsed neutron tools.

Author Contributions All authors contributed to the study conception and design. Material preparation, data collection, and analysis were performed by Xin-Yang Wang, Jun-Yan Chen, and Qiong Zhang. The first draft of the manuscript was written by Xin-Yang Wang, and all authors commented on previous versions of the manuscript. All authors read and approved the final manuscript.

Data Availibility The data that support the findings of this study are openly available in Science Data Bank at https://cstr.cn/31253.11.sciencedb.09071 and https://doi.org/10.57760/sciencedb.09071.

Declarations

Conflict of interest The authors declare that they have no conflict of interest.

References

1. T. Acheampong, G.A. Kemp, Health, safety, and environmental (HSE) regulation and outcomes in the offshore oil and gas industry: a performance review of trends in the United Kingdom Continental Shelf. Saf. Sci. **148**, 105634 (2022). https://doi.org/10.1016/J.SSCI.2021.105634
2. C. Jiang, V. Herwaarden, Ir. Hans Peng et al., International HSE standards on China's largest gas project this paper was presented at the spe international conference on health, safety, and environment in oil and gas exploration and production (Calgary, Alberta, Canada; March 2004). https://doi.org/10.2118/86650-MS
3. A.J. Gale, U.S. Paent, US3104322A, 1958
4. D.V. Ellis, J.M. Singer, *Well Logging for Earth Scientists* (Springer, Netherlands, 2007). https://doi.org/10.1007/978-1-4020-4602-5
5. F. Zhang, S. Hou, X. Jin, Monte carlo simulation on compensated neutron porosity logging in LWD with D-T pulsed neutron

generator. Int. J. Appl. Radiat. Isot. **34**(3), 227–232 (2010). https://doi.org/10.7538/tws.2010.23.01.0015. **(in Chinese)**
6. J.Z. Yang, Monte-carlo simulation method for pulsed neutron density logging during drilling. Well Logging Technol. **33**(6), 521–520 (2009). https://doi.org/10.3969/j.issn.1004-1338.2009.06.005 **(in Chinese)**
7. S.A. Scherbatskoy, U.S. Paent, US2648012A, 1949
8. L. Wang, S. Deng, Y. Fan et al., Detection performance and inversion processing of logging while drilling for extradeep azimuthal resistivity measurements. Petrol. Sci. **16**(5), 1015–1027 (2019). https://doi.org/10.1007/s12182-019-00374-4
9. M. Luycx, T.-V. Carlos, Physics, applications, and limitations of borehole neutron-gamma density measurements. Geophys. **84**, D39–D56 (2019). https://doi.org/10.1190/geo2018-0088.1
10. J.E. Galford, J.A. Quirein, S. Shannon et al., Field test results of a new neutron induced gamma ray spectroscopy geochemical logging tool. This paper was presented at the SPE annual technical conference and exhibition (New Orleans, Louisiana, October 2009). https://doi.org/10.2118/123992-MS
11. W. Wu, A. Yue, M. Tong et al., The calculation and characteristic of elemental sensitivity factor in geochemical logging. Pet. Geosci. **21**, 74–80 (2014). https://doi.org/10.1144/petgeo2013-049
12. W. Wu, N. Wei, L. Li, Quantitative analysis of neutron-capture gamma-ray energy spectra using direct demodulation. Pet. Geosci. **79**, D91–D98 (2014). https://doi.org/10.1144/petgeo2013-049
13. F. Zhang, Q. Zhang, J. Liu et al., A method to describe inelastic gamma field distribution in neutron gamma density logging. Appl. Radiat. Isot. **129**, 189–195 (2017). https://doi.org/10.1016/j.apradiso.2017.08.024
14. R. Pemper, A. Sommer, P. Guo et al., A new pulsed neutron sonde for derivation of formation lithology and mineralogy. This paper was presented at the SPE annual technical conference and exhibition (San Antonio, Texas, USA; September 2006). https://doi.org/10.2118/102770-MS
15. R. Badry, J. Grau, S. Herron et al., High-definition spectroscopy determining mineralogic complexity. Oilfield Rev. **26**, 34–50 (2014)
16. C. Stoller, B. Adolph, M. Berheide et al., Use of $LaBr_3$ for downhole spectroscopic applications. 2011 IEEE Nuclear Science Symposium Conference Record (Valencia, Spain, October 2011). https://doi.org/10.1109/NSSMIC.2011.6154477
17. Q. Zhang, F. Zhang, R.P. Gardner et al., A method for determining density based on gamma ray and fast neutron detection using a Cs_2 $LiYCl_6$ detector in neutron-gamma density logging. Appl. Radiat. Isot. **142**, 77–84 (2018). https://doi.org/10.1016/j.apradiso.2018.09.011
18. O. Shcherbakov, F. Furutaka, S. Nakamura et al., A BGO detector system for neutron-capture studies using radioactive nuclides. Nucl. Instrum. Methods Phys. Res. Sect. A **517**, 269–284 (2004). https://doi.org/10.1016/j.nima.2003.09.042
19. A.G.C. Nair, R. Acharya, K. Sudarshan et al., Determination and validation of prompt k(o)-factors with a monochromatic neutron beam at the Dhruva reactor. Nucl. Instrum. Methods Phys. Res. Sect. A **564**, 2 (2006). https://doi.org/10.1016/j.nima.2006.04.020
20. W. Tang, Q. Zhang, A method for neutron-induced gamma spectra decomposition analysis based on Geant4 simulation. Nucl. Sci. Tech. **33**, 154 (2022). https://doi.org/10.1007/s41365-022-01144-5
21. Y. Wang, Q. Zhang, A characterization study on perovskite X-ray detector performance based on a digital radiography system. Nucl. Sci. Tech. **34**, 69 (2023). https://doi.org/10.1007/s41365-023-01220-4
22. Q. Liang, F. Zhang, J. Fan, A novel gamma-thermal neutron evaluating gas saturation method using pulsed neutron logging tool with dual-CLYC. This paper was presented at the SPWLA 63rd annual logging symposium (Stavanger, Norway, June 2022). https://doi.org/10.30632/SPWLA-2022-0078
23. Y. Wang, J. Liang, Q. Zhang, Development and verification of Geant4-based parallel computing Monte Carlo simulations for nuclear logging applications. Ann. Nucl. Energy **172**, 109079 (2022). https://doi.org/10.1016/j.anucene.2022.109079
24. X. Wang, J. Liang, Y. Li, Hybrid Monte Carlo methods for Geant4-based nuclear well logging implementation. Ann. Nucl. Energy **169**, 108824 (2022). https://doi.org/10.1016/j.anucene.2021.108824
25. X. Wang, Q. Zhang, High-efficiency Monte Carlo simulation based on CADIS method for gamma density measurement. Ann. Nucl. Energy **185**, 109710 (2023). https://doi.org/10.1016/j.anucene.2023.109710
26. Q. Zhang, Source less density measurement using an adaptive neutron induced gamma correction method. Nucl. Sci. Tech. **34**, 125 (2023). https://doi.org/10.1007/s41365-023-01274-4
27. J. Liu, F. Zhang, X. Wang et al., Numerical study to determine formation porosity using boron capture gamma ray technique and MCNP. Appl. Radiat. Isot. **94**, 266–271 (2014). https://doi.org/10.1016/j.apradiso.2014.08.013
28. Q. Zhang, R. Deng, S. Zhang et al., Alternative methods for sourceless density measurement using boron-sleeve gamma detectors. Appl. Radiat. Isot. **174**(4), 109785 (2021). https://doi.org/10.1016/j.apradiso.2021.109785
29. F. Zhang, W. He, X. Wang et al., Compact shielding design of a portable 241Am-Be source. Appl. Radiat. Isot. **128**, 49–54 (2017). https://doi.org/10.1016/j.apradiso.2017.06.033
30. A.M.A. Mostafa, H.M.H. Zakaly, S.A. Al-Ghamdi et al., PbO-Sb_2 O_3 − B_2 O_3-CuO glassy system: evaluation of optical, gamma, and neutron shielding properties. Mater. Chem. Phys. **258**, 123937 (2021). https://doi.org/10.1016/j.matchemphys.2020.123937
31. M. Rashad, H.A. Saudi, M.H. Zakaly et al., Control optical characterization of Ta^{+5}-doped B_2 O_3− Si_2O-CaO-BaO glasses by irradiation dose. Opt. Mater. **112**, 110613 (2021). https://doi.org/10.1016/j.optmat.2020.110613
32. H.A. Saudi, H.O. Tekin, M.H. Zakaly et al., The impact of samarium (III) oxide on structural, optical, and radiation shielding properties of thallium-borate glasses: experimental and numerical investigations. Opt. Mater. **114**, 110948 (2021). https://doi.org/10.1016/j.optmat.2021.110948
33. H.M.H. Zakaly, H.A. Saudi, H.O. Tekin et al., Glass fabrication using ceramic and porcelain recycled waste and lithium niobate: physical, structural, optical, and nuclear radiation attenuation properties. J. Mater. Res. Technol. **15**, 4074–4085 (2021). https://doi.org/10.1016/j.jmrt.2021.09.138
34. J.W. Shin, J.-W. Lee, S. Yu et al., Polyethylene/boron-containing composites for radiation shielding. Thermochim. Acta **585**, 5–9 (2014). https://doi.org/10.1016/j.tca.2014.03.039
35. M.I. Pinilla, A. Hellinger, L.K. Vo et al., Design studies using MCNP6®for an oil well logging prototype tool and a test facility. Radiat. Phys. Chem. **167**, 108393 (2020). https://doi.org/10.1016/j.radphyschem.2019.108393
36. E. Calzada, F. Grünauer, B. Schillinger et al., Reusable shielding material for neutron- and gamma-radiation. Nucl. Instrum. Methods Phys. Res. Sect. A **651**, 77–80 (2011). https://doi.org/10.1016/j.nima.2010.12.239
37. J. Allison, K. Amako, J. Apostolakis et al., GEANT4: simulation toolkit. Nucl. Instrum. Methods Phys. Res. Sect. A **506**, 250–303 (2004). https://doi.org/10.1016/S0168-9002(03)01368-8
38. Boralcan, Boralcan American Materials. https://www.americanelements.com/boralcan-al-b4c-matrix-composite
39. Boron carbide, Boron carbide-Henan Sicheng Abrasives Techo. https://hnabrasive.com/products/Boroncarbide.html

40. K. Ruslan, Mechanical Properties of Boron Carbide (B_4C). Electronic Theses and Dissertations. **81** (2020) https://stars.library.ucf.edu/etd2020/81
41. Aluminum Boron, Master Alloy Supplier | Stanford Advanced Materials. https://www.samaterials.com/aluminum-master-alloy/1622-aluminum-boron-master-alloy.html
42. S.T. Mileiko, *Chapter II - Fibres and Fibrous Composites* (Elsevier Science, Moscow, 1997). https://doi.org/10.1016/S0927-0108(97)80020-3